

Section 4

**Parameterization of important atmospheric
and surface processes,
effects of different parameterizations**

Influence of Cloud Microphysics Scheme and Ice Nuclei on Forecasting a Heavy Snowfall Event in Japan associated with the “South-Coast Cyclones”

Kentaro Araki¹

1: Meteorological Research Institute, Tsukuba, Ibaraki, Japan
e-mail: araki@mri-jma.go.jp

1. Introduction

In winter seasons, extratropical cyclones moving along the south coast of Japan, so-called “South-Coast Cyclones (SCCs)” in Japan, sometimes bring heavy snowfall in the Kanto plain. Numerical models sometimes fail to forecast the track and intensity of the SCCs, and associated heavy snowfall. Araki and Murakami (2015) investigated an extreme heavy snowfall case on 14–15 February 2014 by numerical simulations, focusing on the aerosol indirect effect by ice nuclei, and noted that the concentration of ice nuclei considerably affected snowfall amounts and distribution. In this study, we investigated the influences of cloud microphysics schemes and aerosol indirect effect by ice nuclei on the development of the SCC and snowfall amounts in the Kanto plain in the heavy snowfall case on 8–9 February 2014.

2. Model settings of sensitivity experiments

Numerical simulations were performed by the Japan Meteorological Agency Non-Hydrostatic Model (NHM; Saito et al. 2006) with a horizontal grid spacing of 5 km and a domain of $3,000 \times 2,750$ km covering Japan. The initial and boundary conditions were provided from the 3-hourly JMA mesoscale analysis and the model was run for 72 hours from 21 Japan Standard Time (JST=UTC+9h) on 6 February 2014. In a control run (CNTL), only a bulk cloud microphysics scheme with 2-moment cloud ice, snow, and graupel was used. The other setups were the same as those used in the JMA operational mesoscale model. To estimate the influences of different cloud microphysics schemes, we performed two numerical experiments; one is a bulk cloud microphysics scheme with 2-moment cloud ice and 1-moment snow and graupel (Ice-2m), and the other is that with 1-moment cloud ice, snow, graupel (Ice-1m). A numerical experiment with the same cloud microphysics scheme as in CNTL, but additionally using the Kain-Fritsch convection parameterization (KF), was also performed. To examine the aerosol indirect effect by ice nuclei, two sensitivity experiments with changing coefficients in the formulas of deposition/condensation-freezing-mode ice nucleation (Meyers 1992) and immersion-freezing-mode ice nucleation (Bigg 1955) by factors of 0.1 (IN01) and 10 (IN10) were performed. To compare magnitudes in effects between initial/boundary conditions and cloud microphysics schemes, we performed numerical experiments with initial and boundary conditions derived from the 6-hourly JMA global analysis (GA) and JRA-55 reanalysis (JRA-55; Kobayashi et al. 2015).

3. Influence on the SCC and accumulated snowfall

Firstly, cyclone tracks from 09 JST on 8 February to 21 JST on 9 February (integration time from 36 to 72 hours) simulated by each experiment and analyzed by the JMA were compared (Fig. 1). At 09 JST on 8 February, the centers of the SCC in CNTL and KF were positioned near the SCC center in the analysis. Differences of simulated cyclone tracks from the JMA analysis increased to the east of about 140E (after 15 JST on 8 February), and the SCC in all experiments traveled south of the analyzed track. The differences of cyclone tracks between each experiment were smaller than those between simulated and analyzed tracks after 15 JST on 8 February. The temporal variations of sea level pressure (SLP) in the center of the SCC in each experiment were similar to those of the JMA analysis (Fig. 2a). The differences of SLPs in the center of the SCCs in IN01, KF, GA, and JRA-55 from that in CNTL exceeded 2 hPa (Fig. 2b). These results show that some cloud microphysics schemes, convection parameterization, and initial and boundary conditions introduce comparable uncertainties to the forecasts of the SCC developments.

Secondly, horizontal distributions of snow precipitation amounts from 21 JST on 7 February to 06 JST on 9 February in each experiment were compared (Fig. 3). The simulated distribution in CNTL was similar to that of observations by surface stations (Fig. 3a). Compared with CNTL, both Ice-2m and Ice-1m had the following similar difference; the accumulated snow precipitation amounts were

generally underestimated except in some areas of the Kanto plain (Fig. 3b, c). This difference was caused by the treatment of number concentration of snow, resulting in less surface snowfall amounts in the schemes with 1-moment snow. The positive KF-CNTL difference was found especially on the windward (southern) side of mountainous regions (Fig. 3d), and the similar tendency has been reported in heavy rainfall cases. The results of IN01 and IN10 demonstrate similar differences of snowfall from CNTL especially in heavy snow inland areas (Fig. 3e, f). Since the results of IN01 and IN10 were reported to be opposite features in snowfall in another case (Araki and Murakami 2015), it's suggested that the aerosol indirect effect by ice nuclei would depend on atmospheric conditions such as water vapor supply or temperature even in heavy snowfall cases associated with SCCs. GA and JRA-55 had similar features that were negative and positive differences respectively found in mountainous and plain areas (Fig. 3g, h). In addition, the maximum differences exceeded 20 mm in all experiments.

As a result, it's indicated that cloud microphysics schemes, aerosols indirect effect by ice nuclei, and initial/boundary conditions have similar magnitude of effect on the development of SCCs and associated snowfall in this case. Improvements of not only initial/boundary conditions but also cloud microphysics scheme including the parameterization of ice nuclei are required.

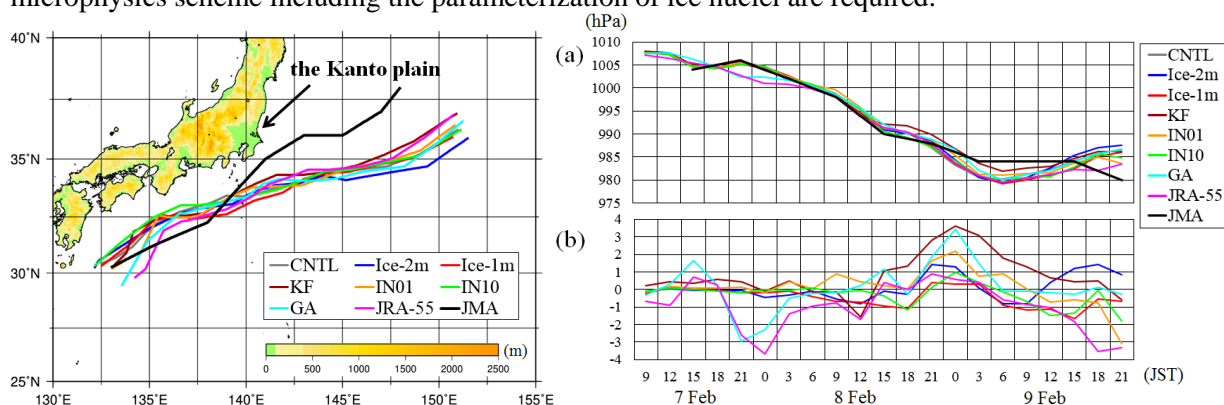


Figure 1. Cyclone tracks in each experiment and the JMA analysis from 09 JST on 8 to 21 JST on 9 February 2014.

Figure 2. Time series of (a) SLPs in the center of the SCCs and (b) their differences from CNTL.

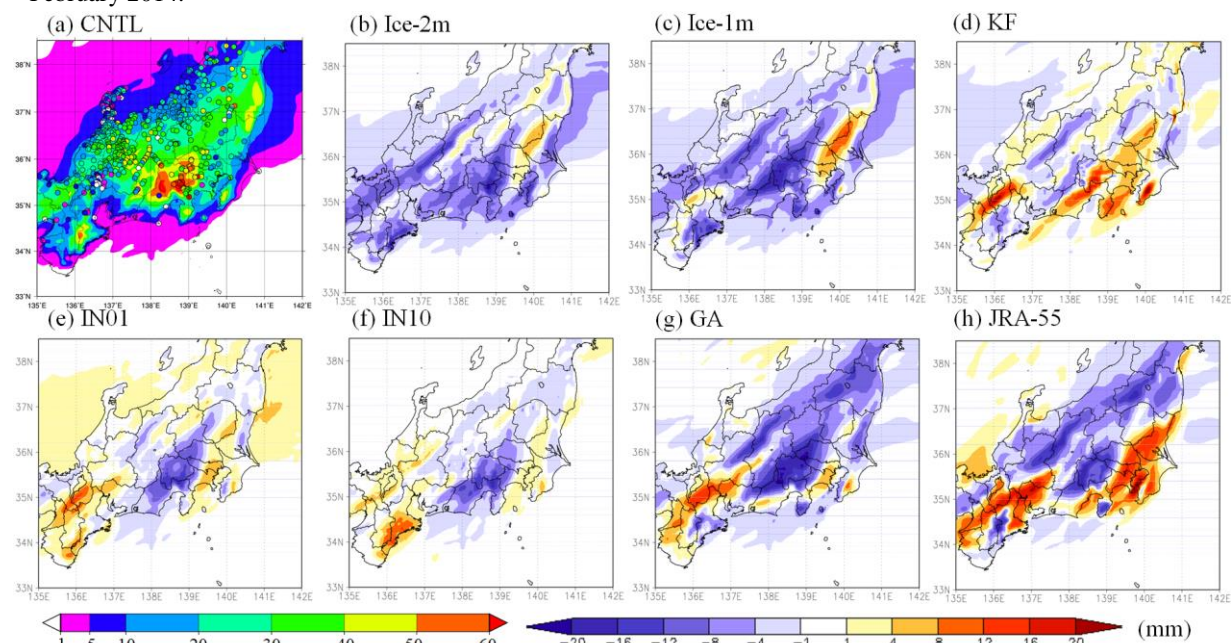


Figure 3. (a) Horizontal distribution of snow precipitation amounts from 21 JST on 7 February to 06 JST on 9 February in CNTL, and the differences from CNTL for each experiments. Circles in (a) denote snowfall observations (cm).

References:

- Araki, K., and M. Murakami, 2015: Numerical simulation of heavy snowfall and the potential role of ice nuclei in cloud formation and precipitation development. *CAS/JSC WGNE Research Activities in Atmospheric and Oceanic Modelling*, **45**, 4.03–4.04.
- Saito, K., T. Fujita, Y. Yamada, J. Ishida, Y. Kumagai, K. Aranami, S. Ohmori, R. Nagasawa, S. Kumagai, C. Muroi, T. Kato, H. Eito, and Y. Yamazaki, 2006: The operational JMA nonhydrostatic mesoscale model. *Mon. Wea. Rev.*, **134**, 1266–1298.

Improvement of MJO prediction and moistening processes for the DYNAMO period

Takuya KOMORI* and Akihiko SHIMPO

Climate Prediction Division, Japan Meteorological Agency, Tokyo, Japan

Email: komori@met.kishou.go.jp

1. INTRODUCTION

Improvement of Madden-Julian Oscillation (MJO) prediction is crucial for medium- to extended-range predictability in light of the link between operational weather and climate predictions. Whilst every effort has been made to improve the MJO prediction skill of the operational Global Spectral Model (GSM) at the Japan Meteorological Agency (JMA), the results of comparison with special observations conducted during the Dynamics of the Madden-Julian Oscillation (DYNAMO) period over the Indian Ocean suggest a lack of skill in the convectively active phase when dry air intrudes into the eastward propagating MJO. Accordingly, a revision of convection and cloud schemes in the GSM with focus on the moistening processes of the MJO is required.

2. REVISED CONVECTION AND CLOUD SCHEMES

The GSM has the prognostic Arakawa-Schubert (AS) convection scheme with a spectral cloud ensemble and prognostic closure, as well as the large-scale cloud scheme with PDF type based on Smith (1990) with some modifications (JMA 2013). In this study, the following modifications were tested for the schemes:

- a) Introduction of new relative-humidity (RH) dependent formulation inspired by Bechtold et al. (2008) for entrainment $\varepsilon(z,t,i)$ in updraft mass flux:

$$\varepsilon(z,t,i) = \varepsilon'(t,i) f(\overline{RH}(z))$$
$$f(\overline{RH}(z)) = (RH_c - 1) \bar{q}_s / \bar{q} + (\bar{q}_s - \bar{q}) / \bar{q} = (RH_c - \overline{RH}(z)) / \overline{RH}(z)$$

where the constant parameter $RH_c = 1.1$, and $\varepsilon'(t,i)$ is diagnosed for each convective plume i at every time step t depending on the environmental profile of moist static energy. \bar{q} and \bar{q}_s are the specific humidity and saturation specific humidity in the environment, respectively.

- b) Implementation of a resolution-dependent parameter on a convective adjustment time scale:

$$\tau = \alpha \tau_0 \times \exp(\beta \cdot n_r)$$

where n_r is the spectral truncation number of the GSM, and τ_0, α, β are constant parameters.

- c) Increased effect of convective momentum transport (CMT) by 20%.

- d) Modification of parameters for cloud ice, resulting in less ice falling to the surface.

3. RESULTS

The results of an experiment (TEST) with the revised convection and cloud schemes were compared to those of an experiment (CNTL) based on operational configuration. The low-resolution version of the GSM (TL479L100) was used for both experiments. Figure 1 shows a situation with dry-air intrusion into the middle troposphere during the DYNAMO period at the ARM (atmospheric radiation measurement) Gan Island site. The new RH-dependent formulation for entrainment and the shorter convective adjustment time scale in TEST reproduced the suppressed convection observed when the dry air intruded. The less amount of detrainment from convection in TEST led to a lower RH value in the middle troposphere as also seen in sonde observation, whereas CNTL exhibited persistent errors with a higher RH value in the middle troposphere due to excessive development of deep convection.

During the DYNAMO period, the MJO was initiated over the Indian Ocean and weakened over the Maritime Continent. Hovmöller plots for velocity potential at 200 hPa in one-month prediction for the MJO (Figure 2) demonstrate significantly improved performance in TEST compared with CNTL for the eastward propagation of the divergent flow. The increased effect of CMT in TEST contributed to a deceleration of the eastward propagation of convectively organized cloud clusters. Due to the effect of RH-dependent entrainment, TEST also reproduced the backward-tilt vertical structure of the MJO and resulted in better distribution of specific humidity in the boundary layer (Figure 3). Wavenumber-frequency spectra with an equatorially symmetric component of the OLR simulated over the period from 2001 to 2007 with TL159L100 using SST climatology (Figure 4) revealed an excessive Kelvin wave peak and a significantly weakened signal for the MJO in CNTL. These values were better in TEST, although there is still room for improvement of spectral strength. Overall, the revision of the convection and cloud schemes shows encouraging results with significant improvement of prediction for many aspects of the MJO and related moistening processes. In future work, the characteristics of error growth depending on GSM horizontal resolution will be investigated toward the operational seamless prediction covering from short-range to seasonal time scales.

REFERENCE

- Bechtold P., M. Kohler, T. Jung, F. Doblas-Reyes, M. Leutbecher, M. Rodwell, F. Vitart and G. Balsamo, 2008: Advances in simulating atmospheric variability with the ECMWF model: From synoptic to decadal timescales. *Q. J. R. Meteorol. Soc.*, **134**, 1337–1351.
- JMA, 2013: Outline of the operational numerical weather prediction at the Japan Meteorological Agency. Appendix to WMO technical progress report on the global data-processing and forecasting system and numerical weather prediction research. 188pp. Available online: <http://www.jma.go.jp/jma/jma-eng/jma-center/nwp/outline2013-nwp/index.htm>
- Smith, R. N. B., 1990: A scheme for predicting layer clouds and their water content in a general circulation model. *Q. J. R. Meteorol. Soc.*, **116**, 435–460.

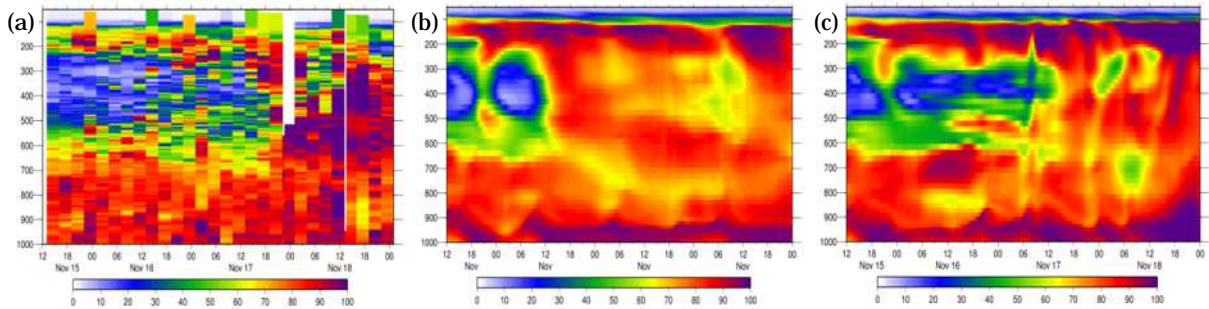


Figure 1. Pressure-time cross section of relative humidity [%] at the ARM Gan Island site for (a) sonde observation and 84-hour simulations of (b) CNTL and (c) TEST with TL479L100 with an initial time of 12 UTC on 15 November 2011

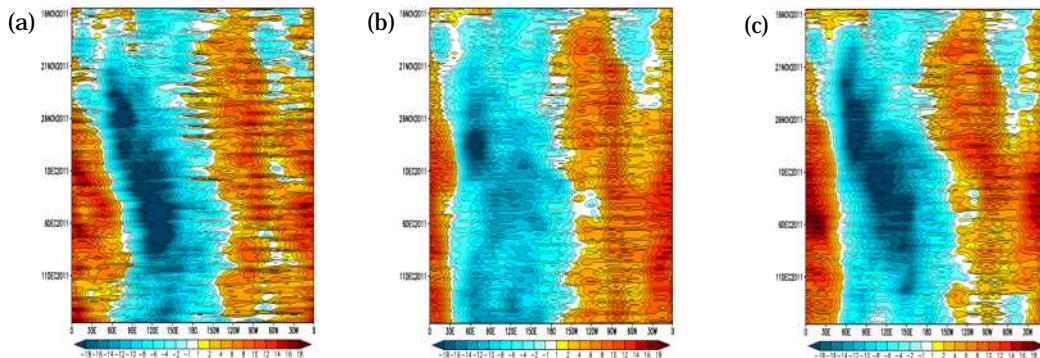


Figure 2. Hovmöller plots of velocity potential at 200 hPa [$10^6 \text{ m}^2 \text{ s}^{-1}$] averaged over $15^\circ\text{S} - 15^\circ\text{N}$: (a) ERA-Interim and one-month simulations of (b) CNTL and (c) TEST with TL479L100 with an initial time of 12 UTC on 15 November 2011

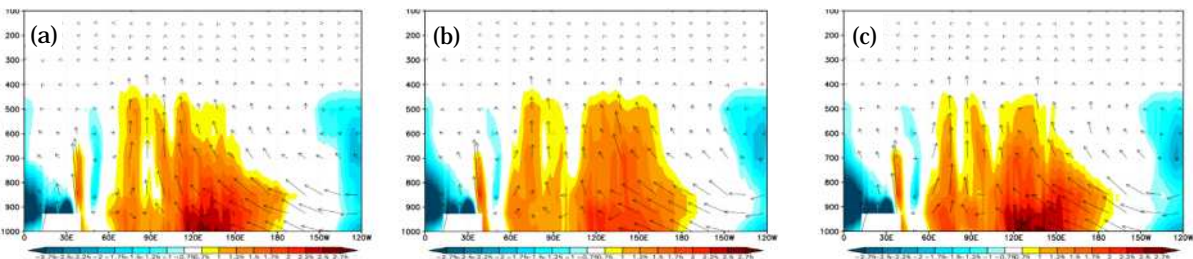


Figure 3. Pressure-longitude cross section of specific humidity [g kg^{-1}] anomaly (shaded) and moisture flux vectors of zonal [$\text{m s}^{-1} \text{ g kg}^{-1}$] and vertical [$\text{Pa s}^{-1} \text{ g kg}^{-1}$] components : (a) operational analysis, (b) CNTL and (c) TEST simulations with TL479L100 72-hour forecast with an initial time of 12 UTC on 26 November 2011

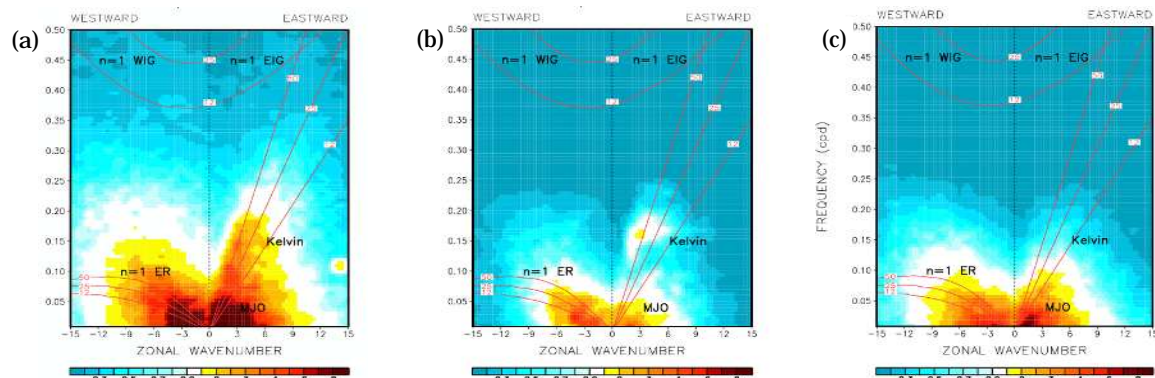


Figure 4. Wavenumber-frequency power spectra with an equatorially symmetric component of the OLR ($15^\circ\text{N} - 15^\circ\text{S}$): (a) NOAA AVHRR, (b) CNTL and (c) TEST simulations over the period from 2001 – 2007 with TL159L100 using SST climatology

The mixed-phase version of moist-air entropy

by Pascal Marquet

Météo-France. CNRM/GMAP. Toulouse. France. *E-mail: pascal.marquet@meteo.fr*

1 Motivations

The specific (per unit mass of *moist-air*) entropy is defined in Marquet (2011, M11) by $s = s_{ref} + c_{pd} \ln(\theta_s)$, where s_{ref} and c_{pd} are two constants. The first- and second-order approximations $(\theta_s)_1$ and $(\theta_s)_2$ of the moist-air entropy potential temperature θ_s have been more recently derived in Marquet (2015, M15).

The aim of this note is to derive the *mixed-phase* version of θ_s , $(\theta_s)_1$ and $(\theta_s)_2$, namely if liquid water and ice are allowed to coexist, with possible under- or super-saturations, with possible supercooled water and with possible different temperatures for dry air and water vapour, on the one hand, condensed water and ice, on the other hand.

2 The mixed-phase definition of θ_s

The specific (per unit mass of *moist-air*) entropy given by (B.1) in M11 is equal to the sum

$$s = q_d s_d + q_v s_v + q_l s_l + q_i s_i, \quad (1)$$

where specific contents in dry-air, water vapor, liquid water and ice (q_d, q_v, q_l, q_i) act as weighting factors. The common temperature T for the dry air and water vapour entropies (s_d, s_v) is possibly different from those T_l or T_i for liquid water or ice entropies (s_l, s_i), respectively.

Without loss of generality, the moist-air entropy given by (1) can be rewritten in a way similar to (B.2) in M11, leading to

$$s = q_d s_d + q_t s_v + q_l (s_l^* - s_v) + q_i (s_i^* - s_v) + q_l (s_l - s_l^*) + q_i (s_i - s_i^*), \quad (2)$$

where $q_t = q_v + q_l + q_i$ is the total water content.

The first difference from the result derived in M11 is due to s_l and s_i which must be computed in the second line of (2) at temperatures T_l and T_i , respectively, whereas s_l^* and s_i^* are computed at the common temperature T for the two gaseous species. The second line of (2) can thus be computed with $s_l - s_l^* = c_l \ln(T_l/T)$ and $s_i - s_i^* = c_i \ln(T_i/T)$, where the reference entropies $(s_l)_r$ and $(s_i)_r$ have no impact.

The other difference concerns the bracketed terms in (B.7) in M11, namely the term $R_v [q_l \ln(H_l) + q_i \ln(H_i)]$, where $H_l = e/e_{sl}$ and $H_i = e/e_{si}$ are the relative humidities with respect to liquid water and ice, respectively. These bracketed terms no longer cancel out if liquid water and ice are allowed to coexist, and/or with possible under- or super-saturations.

These differences with respect to non-mixed phase results of M11 lead to the following mixed-phase generalisation of θ_s :

$$\theta_s = \left[\theta \exp\left(-\frac{L_v q_l + L_s q_i}{c_{pd} T}\right) \right] \exp(\Lambda_r q_t) \left(\frac{T}{T_r}\right)^{\lambda q_t} \left(\frac{p}{p_r}\right)^{-\kappa \delta q_t} \left(\frac{r_r}{r_v}\right)^{\gamma q_t} \frac{(1+\eta r_v)^{\kappa(1+\delta q_t)}}{(1+\eta r_r)^{\kappa \delta q_t}} (H_l)^{\gamma q_l} (H_i)^{\gamma q_i} \left(\frac{T_l}{T}\right)^{c_l q_l/c_{pd}} \left(\frac{T_i}{T}\right)^{c_i q_i/c_{pd}}. \quad (3)$$

The bracketed terms in the first line of (3) is the ice-liquid version of the Betts' potential temperature θ_l , where the latent heats L_v and L_s depends on T . The whole first line of (3), including the term $\exp(\Lambda_r q_t)$ which depends on the Third-Law reference values $(s_v)_r$ and $(s_d)_r$, forms the first-order approximation $(\theta_s)_1$. Some of the terms in the second line of (3) are used in M15 to derive the second-order approximations $(\theta_s)_2$.

The third line of (3) is made of the four new *mixed-phase correction terms*. These terms are clearly equal to unity for the non-mixed phase conditions retained in M11, namely if $T_l = T_i = T$, $H_l = 1$ for $q_l \neq 0$ and $H_i = 1$ for $q_i \neq 0$.

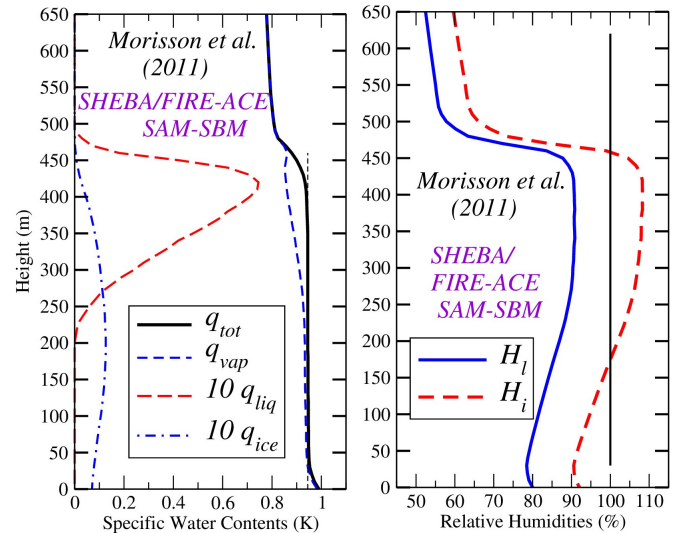


Figure 1: The vertical profile of water species contents and relative humidities corresponding to the yellow curve (SAM-SBM) in Figure 7 of Morisson *et al.* (2011).

3 Some Numerical results

The impact of the two new mixed-phase terms $(H_l)^{\gamma q_l}$ and $(H_i)^{\gamma q_i}$ in (3) are evaluated by using SHEBA/FIRE-ACE vertical profiles for $(\theta_l, q_t, q_l, q_i)$ depicted in Figure 7 of Morisson *et al.* (2011).

The profiles of (q_t, q_v, q_l, q_i) and (H_l, H_i) are shown in Fig.1. The contents in liquid water and ice are small (mind the factor 10!), but they are associated with relative humidities mostly different from 100 %. One may thus expect the factors $(H_l)^{\gamma_{q_l}}$ and $(H_i)^{\gamma_{q_i}}$ to be (slightly) different from unity. The vertical profiles

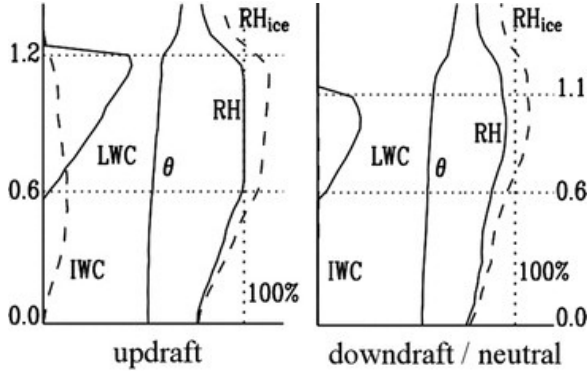


Figure 2: The conceptual model depicted in Shupe et al. (2008) showing typical values for water species contents, θ and relative humidities in autumn Arctic mixed-phase stratiform clouds (for updraft and downdraft regions).

$H_l(z)$ and $H_i(z)$ shown in Fig.1 are similar to those described in Fig.2 for Arctic mixed-phase clouds, with liquid and ice water content typical of updrafts and relative humidities typical of downdrafts.

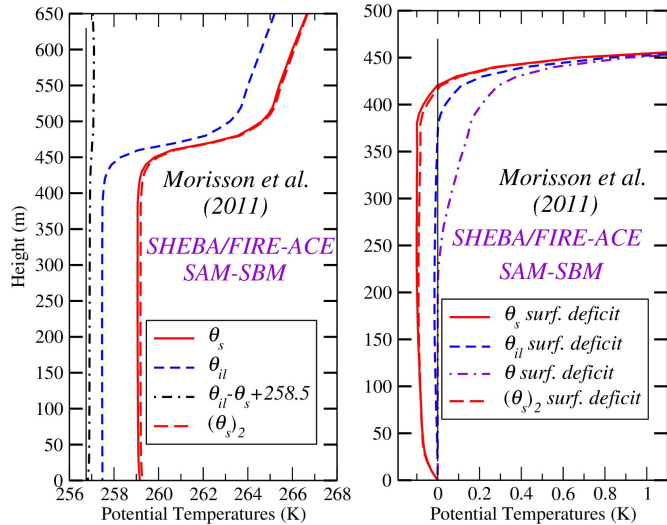


Figure 3: Same as in Fig. 1 but for vertical profiles (left) and surface deficit values (right) for several potential temperatures: θ_s given by (3); θ_{il} defined in Tripoli and Cotton (1981); $\theta = T(p_0/p)^{(R_a/c_{pd})}$; the second-order value $(\theta_s)_2$ defined in M15 but multiplied by the third line of (3).

The paradigm for describing and simulating mixed-phase cloud is to consider that the ice-liquid potential temperature θ_{il} is a conservative variables, where θ_{il} defined in Tripoli and Cotton (1981) is similar to the bracketed terms in the first line of (3), except that the latent heats $L_v(T_0)$ and $L_s(T_0)$ are computed at the triple-point temperature $T_0 = 273.16$ K (not at T).

The conserved (namely constant) feature observed for θ_{il} in the PBL of Fig.3 is likely due to the choice

of the ice-liquid water static energy h_L as a prognostic variables in the SAM-SBM runs, where $h_L = c_{pd}T + gz - L_v(T_0)q_l - L_s(T_0)q_s$ is clearly a proxy for θ_{il} .

Differently, it is shown in Fig.3 that the mixed-phase moist-air entropy value θ_s given by (3) is not conserved (with $(\theta_s)_2$ being indeed a good approximations of θ_s). This may be interpreted as an impact of the term $\exp(\Lambda_r q_t)$ in the first line of (3) and due to changes in q_t shown in Fig.1 close to the ground (below 50 m).

This impact of q_t was missing in the definition of θ_{il} and in the approximate integration of the first and the second laws of thermodynamics derived in Dutton (1976, see before Eq.30, p.284, in the 1986 edition).

The “equivalent” version θ_{eil} defined in Tripoli and Cotton (1981) includes a factor $\exp[(L_v(T_0)q_t)/(c_{pd}T)]$ which depends on q_t , where $L_v(T_0)/(c_{pd}T) \approx 9$. This factor is however different from the one $\exp(\Lambda_r q_t)$ appearing in θ_s given by (3), where $\Lambda_r \approx 6$ depends on the Third-Law reference values $(s_v)_r$ and $(s_d)_r$. Only θ_s with $\Lambda_r \approx 6$ is an *equivalent* of the moist-air entropy.

4 Conclusions

The search for “conserved” variables based on approximations of the moist-air entropy (function or equation) should be replaced by the use of the *conservative* variables θ_s given by (3) which is a true *equivalent* variable.

A model using the mixed-phase version (3) for θ_s as a prognostic variable, including for turbulent and mass-flux mixing processes, could lead to more accurate results. The impacts of the last two terms of (3) are to be investigated (ex. for supercooled water).

References

- Dutton J. A. (1986). The Ceaseless Wind. *Dover Publications*. 617 pages.
- Marquet P. (2011, M11). Definition of a moist entropic potential temperature. Application to FIRE-I data flights. *Q. J. R. Meteorol. Soc.* **137** (656): p.768–791.
- Marquet P. (2015, M15). An improved approximation for the moist-air entropy potential temperature θ_s . *WGNE Blue-Book*. <http://arxiv.org/abs/1503.02287>
- Morrison H. et al. (2011). Intercomparison of cloud model simulations of Arctic mixed-phase boundary layer clouds observed during SHEBA/FIRE-ACE *J. Adv. Model. Earth Syst. (JAMES)* **3** (2): p.1942-2466.
- Shupe M. D. et al. (2008). Vertical Motions in Arctic Mixed-Phase Stratiform Clouds. *J. Atmos. Sci.* **65** (4): p.1304-1322.
- Tripoli G. J., Cotton W. R. (1981). The Use of Ice-Liquid Water Potential Temperature as a Thermodynamic Variable In Deep Atmospheric Models. *Mon. Wea. Rev.* **109** (5): p.1094–1102.

The implementation of NEMS GFS Aerosol Component (NGAC) Version 2: Global aerosol forecasting at NCEP using satellite-based smoke emissions

Jun Wang^{1,2}, Sarah Lu³, Xiaoyang Zhang⁴, Shobha Kondragunta⁵, Arlindo da Silva⁶, Jeff McQueen², Partha Bhattacharjee^{2,3}, Shrinivas Moorthi², Andy Harris^{5,7}, Prabhat Koner^{5,7}, Yu-Tai Hou², and Vijay Tallapragada²

¹: NCEP/EMC, ²: IMSG, ³: University at Albany, State University of New York, ⁴: South Dakota State University, ⁵: NESDIS/STAR, ⁶: NASA GMAO, ⁷: ESSIC/UMD

Email: jun.wang@noa.gov

1. Introduction

Atmospheric aerosols have profound impact on weather, climate, human health, and the economy. The National Centers for Environmental Prediction (NCEP) has partnered with NASA's Global Modeling and Assimilation office (GMAO) and the NOAA/NESDIS Center for Satellite Applications and Research (STAR) to develop a global aerosol model NEMS GFS Aerosol Component (NGAC) to predict the distribution of atmospheric aerosols (Lu *et al.*, 2016). The development of a global aerosol forecast system paved the way to a full aerosol modeling system with forecast model and aerosol data assimilation capability at NCEP. The overarching goals for developing the global aerosol forecasting and data assimilation capabilities are to improve weather forecasts and climate predictions, provide boundary conditions for regional air quality models, sea surface temperature retrievals and UV index forecasts, as well as to serve a wide range of stakeholders such as health professionals, aviation authorities and policy makers.

2. Model description

The NGAC consists of two key modeling components: the Global Spectral Model (GSM) within the NOAA Environmental Modeling System (NEMS) architecture and the on-line aerosol module based on the Goddard Chemistry Aerosol Radiation and Transport (GOCART) model (Colarco *et al.*, 2010). NGAC Version 1.0 has been providing 5-day dust forecasts at 1°x1° resolution on a global scale, once per day at 0000 Coordinated Universal Time (UTC), since September 2012. An NGAC upgrade (NGAC V2) is planned to be implemented into operations in 2016. This implementation extends the aerosol species from dust only to multiple species including dust, sea salt, sulfate, organic carbon and black carbon aerosols to provide a more complete global aerosol forecast. The major meteorological model physics updates include McICA radiation package in Rapid Radiative Transfer Model (RRTM), Eddy-Diffusivity Mass-Flux (EDMF) Planetary Boundary Layer (PBL) scheme and a Noah land surface update for canopy height scheme, soil moisture nudge and roughness length.

With support from the Joint Center for Satellite Data Assimilation (JCSDA), the NCEP-STAR-GMAO team developed a near-real-time (NRT) smoke emission product on a global scale. The smoke emissions are blended from STAR's Global Biomass Burning Emission Product from a constellation of geostationary satellites (GBBEP, Zhang *et al.*, 2012) and GSFC's Quick Fire Emissions Data Version 2 from a polar orbiting sensor, providing daily global emission fluxes for CO₂, CO, OC, BC, PM_{2.5}, and SO₄.

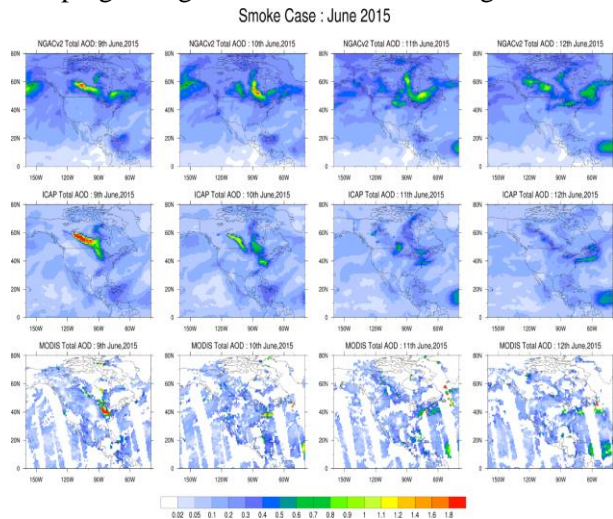


Fig.1 Total AOD from NGAC V2 (top panels), the ICAP MMEs (middle panels), and MODIS (bottom panels) during Jun 9-12, 2015.

3. Results

A two year retrospective run has been conducted using NGAC V2 to provide multi-species aerosol simulations. The results show that NGAC V2 has comparable forecast skill for dust forecasts and captures the major pollution events over Asia and North America and matches closely with MODIS on total AOD. Figure 1 shows elevated aerosol optical depth (AOD) stretching from Canada to the Great Lakes and the Mid-Atlantic region during June 9-12, 2015. The increase in AOD corresponds to widespread fire activity in Canada that traveled across the continent throughout the period. AOD simulated by NGAC V2 is consistent with the International Cooperative for Aerosol Prediction Multi-Model Ensemble as well as observations from the space-borne Moderate Resolution Imaging Spectroradiometer (MODIS) sensor.

4. Applications

The implementation of NGAC V2 provides a full suite of 2-dimensional (2-D) and 3-dimensional (3-D) aerosol products for various downstream applications. Figure 2 shows aerosol information application in physical deterministic retrievals of Sea-Surface Temperature (SST). Aerosol column density (ACD) of all aerosols is included in the state vector for the MODIS-Aqua SST retrieval. Additional channels available for MODIS, combined with a 3-element reduced state vector, offers the prospect of testing a variant of the Truncated Total Least Squares (TTLS) approach. A comparison between results for the 2-component [SST, total column water vapor (TCWV)] for the Modified Total Least Squares (MTLS, Koner *et al.*, 2015) algorithm and 3-component [SST, TCWV, ACD] state vectors is shown in Figure 2. It can be seen that the RMSE (dashed standard deviation lines in Figure 2) is improved noticeably when ACD is a retrieved parameter. A further consequence of including ACD in the state vector is that algorithm sensitivity is significantly improved. This is demonstrated by the increase in the degree of freedom in retrieval (DFR) values to 0.75 and above.

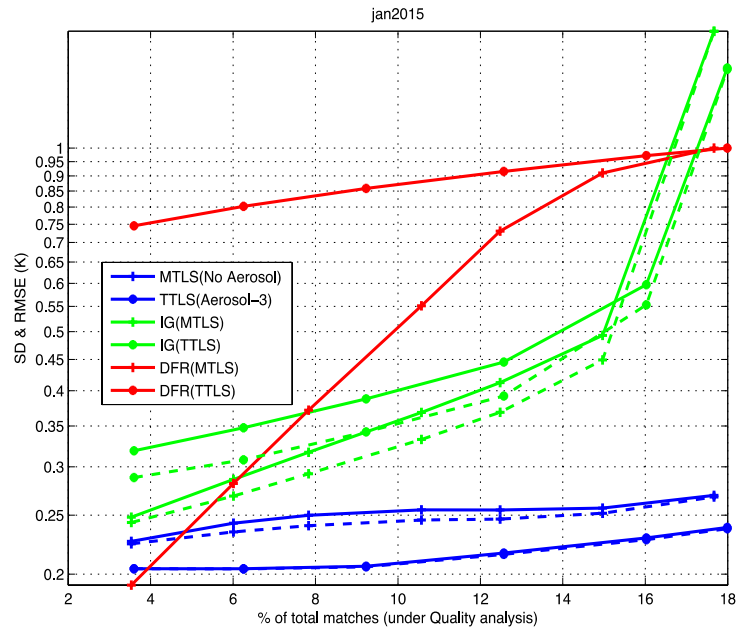


Figure 2. Comparison of retrieval accuracy (blue lines) and algorithm sensitivity (Degrees of Freedom in Retrieval, red lines) of MTLs (crosses) without aerosol and Truncated Total Least Squares (solid circles) using aerosol optical depth in the state vector for MODIS-Aqua data for January 2015. Evaluation is done against *i*Quam buoy data. Initial Guess (IG) SST accuracy (green lines) is also shown.

References

- Colarco, P., A. da Silva, M. Chin, and T. Diehl, 2010. Online simulations of global aerosol distributions in the NASA GEOS-4 model and comparisons to satellite and ground-based aerosol optical depth, *J. Geophys. Res.*, 115, D14207, doi:10.1029/2009JD012820.
- Koner, P.K., A. Harris, E. Maturi, 2015. A Physical Deterministic Inverse Method for Operational Satellite Remote Sensing: An Application for Sea Surface Temperature Retrievals, *IEEE Trans. Geosci. Remote Sens.*, 53, 5872-5888.
- C.-H. Lu, A. da Silva, J. Wang, S. Moorthi, M. Chin, P. Colarco, Y. Tang, P. S. Bhattacharjee, S.-P. Chen, H.-Y. Chuang, H.-M. H. Juang, J. McQueen, and M. Iredel: The implementation of NEMS GFS Aerosol Component (NGAC) Version 1.0 for global dust forecasting at NOAA/NCEP, *Geosci. Model Dev. Discuss.*, doi:10.5194/gmd-2015-236, 2016
- Zhang, X., S. Kondragunta, J. Ram, C. Schmidt, and H-C Huang, 2012. Near-real-time global biomass burning emissions products from geostationary satellite constellation, *J. Geophys. Res.*, 117, D14201, doi:10.1029/2012JD017459.

Development of a two-moment three-ice bulk microphysical model for ice

Yoshinori Yamada

Meteorological Research Institute, Tsukuba, Ibaraki, 305-0052, JAPAN

E-mail: yyamada@mri-jma.go.jp

1. Introduction

A two-moment three-ice bulk microphysical model for ice is developed, as one of the options of the Japan Meteorological Agency non-hydrostatic model (hereafter, JMA-NHM: e.g. Saito et al. 2006), in order to improve the representation of snow clouds and the associated snowfalls. It was found that the current bulk microphysical model did not sometimes represent heavy snow fall events in the Ishikari Plane in Hokkaido very well. This deficiency implies the necessity of the improvement in the bulk microphysical model. Indeed, the current ice-phase processes in the three-ice bulk microphysical model (Ikawa and Saito 1991; Murakami 1990) integrated in the JMA-NHM have been used for a long time without substantial updates. This paper briefly describes the outline of the new bulk microphysical model and results of the preliminary test.

2. Outline of the new microphysical model

The newly developed bulk microphysical model predicts both the mixing ratios and the number concentrations of cloud ice, snow, and graupel. The model incorporates a bin-like approach in the graupel formation. Significant features of the new model are as follows: (a) Size distributions are represented by Gamma function as $n(D) = n_0 D^\nu \exp(-\lambda D)$, where D is the size of particles; (b) Mass-size relations are expressed by power laws as $m = \alpha_m D^{\beta_m}$; (c) Cloud ice whose size is larger than a prescribed value is converted into snow as in Harrington et al (1995). For this conversion calculation, a fast and accurate program for calculating the incomplete Gamma function is implemented; (d) Formation of graupel by riming of cloud ice and snow is modeled by introducing a bin-like idea, in which the graupel formation is determined by the riming rates of cloud ice and snow. Their size distributions are divided into certain number of bins first, then riming rates of particles (cloud ice or snow) in each bin are computed based on the continuous growth model. The resultant riming rate of a single particle is used to determine the occurrence of graupel. Two different thresholds for the riming rate are prescribed for each of cloud ice and snow. When a calculated riming rate exceeds the upper threshold, all particles in the bin considered are converted to graupel. For the riming rate lying between the two thresholds, a portion of the particles in the bin is transferred to graupel. The riming rate falling below the lower threshold leads to the riming of cloud ice and snow without graupel formation; (e) The aggregation of cloud ice and snow is modeled by a strict solution expressed by Gamma and Gauss hypergeometric functions, in which temperature-dependent collection efficiencies are employed; (f) When the collision between cloud ice and rain produces too much graupel, the bin-like approach as the above-mentioned graupel formation is applied to the interaction between these two species.

3. Results of a preliminary test

The new bulk microphysical model described in section 2 was tested for a heavy snowfall event at and around Sapporo in Hokkaido, Japan, occurred on December 15, 2014. This snowfall was brought about a band-like snow clouds (Fig. 1). Daily precipitation and the daily accumulated snow fall amount at Sapporo Observatory were 25 mm in water equivalence and 39 cm, respectively. Maximum accumulated precipitation for three hours was 10 mm in water equivalent from 16 to 19 JST at this observatory.

Experiments were carried out by employing

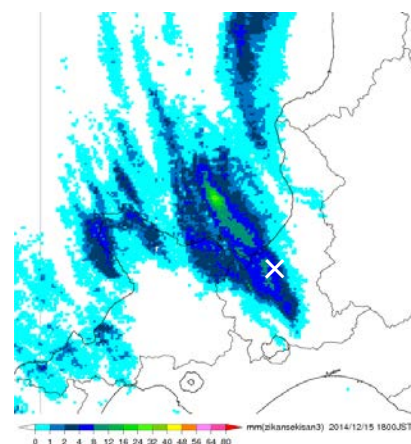


Figure 1. Accumulated precipitation for three hours (shaded area) between 16 and 18 JST from JMA radars. The position of Sapporo is marked by a cross mark. Light blue color indicates precipitation less than 1 mm in water equivalent.

JMA-NHM at a 1-km horizontal resolution for a domain size of 1000 km x 1000 km centered at the location of Sapporo city in order to investigate a performance of the new model relative to the current one. Number of vertical layers was 60, and the top of the model domain was set to 21.8 km. The model run started at the initial time of 00 UTC on Dec. 15 up to 9 forecast hour. The initial and boundary conditions were supplied from the meso analysis of JMA. Except for the bulk microphysical models, other model setting was common to all experiments. No convective parameterization was used, and the turbulent model was Mellor-Yamada-Nakanishi-Niio level 3. For the new microphysical model, the following parameters were tentatively used; the parameters of ν in the size distributions were set equal to 0.5, 2, and 3 for cloud ice, snow, and graupel, respectively; mass-power-laws for broad branches and snowflakes were adopted for cloud ice and snow, respectively; velocity-power law for dendrites was employed for both cloud ice and snow. The mass-size and velocity-size relations for graupel were the same as in Saito et al (2006).

Figure 2 shows simulated precipitation fields from the new and current models. An area of large amount of precipitation exhibits an elongated band pattern in the north-northwest and south-southeast direction for the both models. In particular, the precipitation area associated with the new model is much wider, like that of the radar-derived one shown in Fig. 1 although there is a slight difference in time between the model and the observation. Indeed, a heavy snowfall at Sapporo as well as less intense precipitation in its surrounding area are reproduced very well. The preliminary tests suggest that the new model may have better performance for the snowfall forecast than the current one, and that the snowfall forecast may be sensitive to the microphysical model.

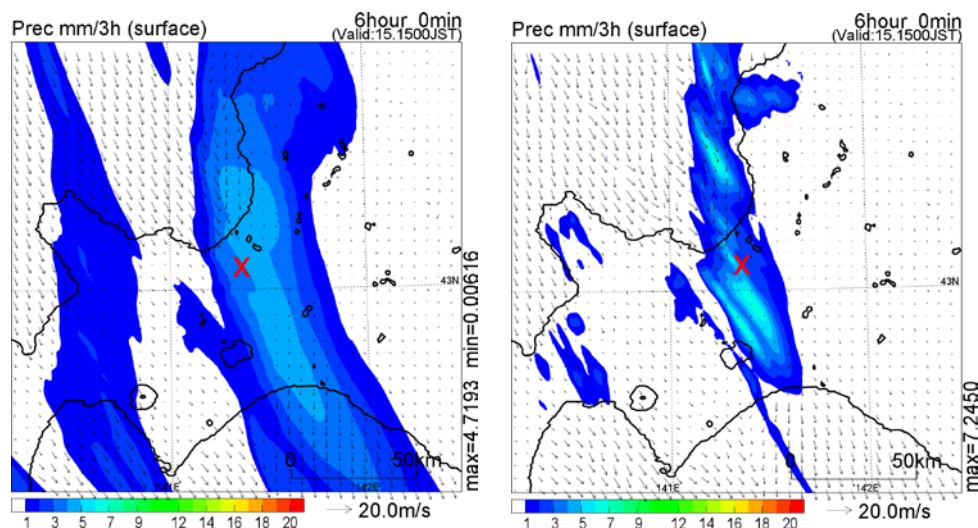


Figure 2. Accumulated precipitation in water equivalence for three hours between 3 and 6 forecast hour is indicated by shading. The left and right panels correspond to the new and current bulk microphysical models, respectively. The position of Sapporo city is shown by a cross mark. The arrows show surface wind.

Acknowledgements

This work was supported by MEXT KAKENHI Grant Number 26242036.

The program for computing the incomplete Gamma function was developed in the cooperative study on photovoltaic power generation between Meteorological Research Institute and National Institute of Advanced Industrial Science and Technology.

References

- Ikawa, K., and K. Saito, 1991: "Description of a nonhydrostatic model developed at the forecast research department of the MRI." Technical reports of the Meteorological Research Institute, No. 28.
- Harrington, J. Y., M. P. Meyers, R. L. Walko, and W. R. Cotton, 1995: Parameterization of ice crystal conversion processes due to vapor deposition for mesoscale models using double-moment basis functions. Part I: Basic formulation and parcel model results. *J. Atmos. Sci.*, **52**, 4344-4366.
- Murakami, M., 1990: Numerical modeling of dynamical and microphysical evolution of an isolated convective cloud --- The 19 July 1981 CCOPE cloud. *J. Meteor. Soc. Japan*, **68**, 107-128.
- Saito, K., T. Fujita, Y. Yamada, J. Ishida, Y. Kumagai, K. Aranami, S. Ohmori, R. Nagasawa, S. Kumagai, C. Muroi, T. Kato, H. Eito, and Y. Yamazaki, 2006: The Operational JMA Nonhydrostatic Mesoscale Model. *Mon. Wea. Rev.*, **134**, 1266-1298.